JOURNAL OF SYNCHROTRON RADIATION
ISSN 1600-5775

First high-pressure XAFS results at the bending-magnet-based energy-dispersive XAFS beamline BL-8 at the Indus-2 synchrotron facility

Debdutta Lahiri,[a]* Ashutosh Dwivedi,[b] R. Vasanthi,[a] S. N. Jha[b] and Nandini Garg[a,c]*

[a]High Pressure and Synchrotron Radiation Physics Division, Bhabha Atomic Research Centre, Mumbai 400085, India, [b]Atomic and Molecular Physics Division, Bhabha Atomic Research Centre, Mumbai 400085, India, and [c]Training School Complex, Homi Bhabha National Institute, Anushaktinagar, Mumbai 400094, India. *Correspondence e-mail: dlahiri@barc.gov.in, nandini@barc.gov.in

Received 31 January 2020
Accepted 4 May 2020

Edited by S. M. Heald, Argonne National Laboratory, USA

Keywords: high-pressure XAFS; energy-dispersive XAFS.

Supporting information: this article has supporting information at journals.iucr.org/s

The static focusing optics of the existing energy-dispersive XAFS beamline BL-8 have been advantageously exploited to initiate diamond anvil cell based high-pressure XANES experiments at the Indus-2 synchrotron facility, India. In the framework of the limited photon statistics with the 2.5 GeV bending-magnet source, limited focusing optics and 4 mm-thick diamond windows of the sample cell, a (non-trivial) beamline alignment method for maximizing photon statistics at the sample position has been designed. Key strategies include the selection of a high X-ray energy edge, the truncation of the smallest achievable focal spot size to target size with a slit and optimization of the horizontal slit position for transmission of the desired energy band. A motor-scanning program for precise sample centering has been developed. These details are presented with rationalization for every step. With these strategies, Nb *K*-edge XANES spectra for Nb_2O_5 under high pressure (0–16.9 GPa) have been generated, reproducing the reported spectra for Nb_2O_5 under ambient conditions and high pressure. These first HPXANES results are reported in this paper. The scope of extending good data quality to the EXAFS range in the future is addressed. This work should inspire and guide future high-pressure XAFS experiments with comparable infrastructure.

1. Introduction

The X-ray absorption based 'X-ray absorption fine structure' (XAFS) technique (Koningsberger & Prins, 1988) is unique for its (i) simultaneous determination of the chemical state (XANES portion of the spectra) (Pantelouris *et al.*, 1995; Brown *et al.*, 1977; Lu *et al.*, 1992) and structure of materials, with unparalleled application in catalysis (Bare *et al.*, 2010; Chen *et al.*, 2005; Stoupin *et al.*, 2006; Misra *et al.*, 2008), (ii) element-specificity that resolves information between different sites (Lahiri *et al.*, 2005; Haskel *et al.*, 1999), and (iii) sensitivity to amorphous structure (Lahiri *et al.*, 2014; Suzuki *et al.*, 2002; Parsons *et al.*, 2011). The application of XAFS has pervaded several domains (Lahiri *et al.*, 2005, 2014; Doudna *et al.*, 2003; Suzuki *et al.*, 2002; Chen *et al.*, 2005; Meneghini *et al.*, 1997; Haskel *et al.*, 1999; Impellitteri *et al.*, 2007; Stoupin *et al.*, 2006; Parsons *et al.*, 2011), including matter under high pressure which is the subject of the present paper. High-pressure XAFS (HPXAFS) studies derive importance from understanding the conditions of inaccessible regions of the Earth (Andrault *et al.*, 1995; Miyauchi *et al.*, 2002; Aquilanti *et al.*, 2015; Hong *et al.*, 2013; Boccato *et al.*, 2017), tuning magnetic/electronic/thermal properties of materials (Hemley, 2000; Itie *et al.*, 1989; Ding *et al.*, 2009; Bastea *et al.*, 2001; Haskel *et al.*,

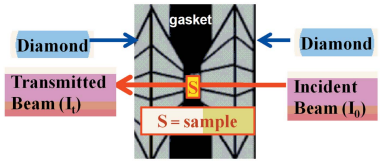

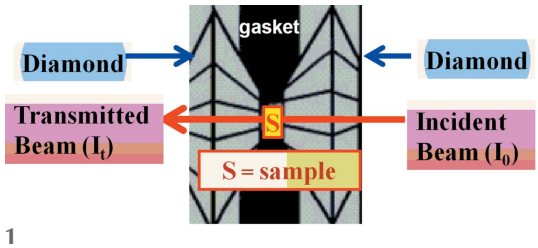

Figure 1
Geometry of the diamond anvil cell with respect to the X-ray beam. The sample S is defined by the gasket and sandwiched between diamond anvils on two sides. The incident beam I_0 enters through the diamond into sample S, and the post-sample transmitted beam I_t exits through the other diamond.

2011; Joseph *et al.*, 2017; Morozoma *et al.*, 2019) and synthesis of novel functional materials (Liu *et al.*, 2018; Liu, 2011; Walsh & Freedman, 2018; McMillan, 2002, 2003; Machon *et al.*, 2018; Zeng *et al.*, 2010). This has motivated the initiation of HPXAFS experiments in India, utilizing the domestic (2.5 GeV) Indus-2 synchrotron facility (http://www.rrcat.gov.in). [The HPXRD beamline is already in use at Indus-2 (http://www.rrcat.gov.in/technology/accel/srul/beamlines/edxrd.html)].

HPXAFS experiments are amongst the most challenging due to the involvement of a diamond anvil cell (DAC) and the statistical and systematic noise it induces. A DAC consists of two diamond anvils, pressing a microgram-sized sample from opposite directions (Eremets, 1996; Shen & Mao, 2017; Garg, 2017; Sharma & Garg, 2017). The sample is contained within a micrometre-sized hole, drilled in the gasket between diamond anvils. The geometry of a DAC with respect to the X-ray beam direction is demonstrated in Fig. 1: diamond anvils serve as X-ray windows for incident (I_0) and transmitted (I_t) beam; XAFS is measured by $\mu = \ln(I_0/I_t)$. Sample size is small ($D \leq$ 250 µm) in order to raise pressure ($P \propto 1/D^2$) (Ramanan *et al.*, 2015). This configuration poses two challenges for XAFS. Firstly, a large X-ray beam size would create a footprint on the diamond; if the Bragg diffraction condition is satisfied, the beam will generate strong diffraction peaks from diamond which will be superimposed on the XAFS spectra (Hong *et al.*, 2009). Deglitching diffraction peak from XAFS spectra during data processing is non-trivial; replacing the peaks with a linear or polynomial interpolation is likely to distort the data. Thus, it is imperative to minimize the number of diffraction peaks during the experiment itself. This necessitates either minimizing the footprint of the beam on the diamond with a small and mechanically stable beam (Pascarelli *et al.*, 2004, 2006, 2016; Baudelet *et al.*, 2011; Pascarelli & Mathon, 2010; Mathon *et al.*, 2004, 2015; Kulow *et al.*, 2019; Kantor *et al.*, 2018) or replacing crystalline diamonds with (expensive) polycrystalline diamonds (Ishimatsu *et al.*, 2012). The second problem with the DAC is a weakening of the signal-to-noise ratio (*i.e.* poor statistics) due to X-ray absorption within the diamond windows (Ramanan *et al.*, 2015). This could result in incorrect normalization for I_0/I_t; further, the Fourier transform of the statistical noise could generate spurious peaks in *r*-space that interfere with the real structure. The problem could be compensated by high photon flux, so that HPXAFS beamlines are preferably commissioned on undulators (Baudelet *et al.*, 2011; Pascarelli & Mathon, 2010; Pascarelli *et al.*, 2016) or on bending magnets with advanced focusing optics (Mathon *et al.*, 2015). An alternative solution is tailoring (perforation/thinning) of the diamonds to reduce the effective thickness (Dadashev *et al.*, 2001; Soignard *et al.*, 2010; Boehler, 2006; Bassett *et al.*, 2000; Haskel *et al.*, 2007).

For the HPXAFS setup in India, we exploited the static focused beam of the pre-existing energy-dispersive XAFS (EDXAFS) beamline BL-8 at Indus-2 (Bhattacharyya *et al.*, 2009). A schematic layout of BL-8 is depicted in Fig. 2(*a*). The sequence of beam source, polychromator (CC), sample stage at S_0 and position-sensitive detector constitutes the backbone configuration of these experiments [Fig. 2(*a*)]. White synchrotron beam is incident on an elliptical Si(111) crystal polychromator (CC), such that the source and sample are located at two focii of the ellipse (Das *et al.*, 1999). The polychromator, preset at the Bragg angle corresponding to the desired photon energy (E_0), diffracts a band of energy ΔE around E_0. The energy band is spatially dispersed in the horizontal plane and converges at the focal point (S_0), where the sample is positioned. Due to the elliptic geometry, the focal spot position is stable against beam fluctuations along

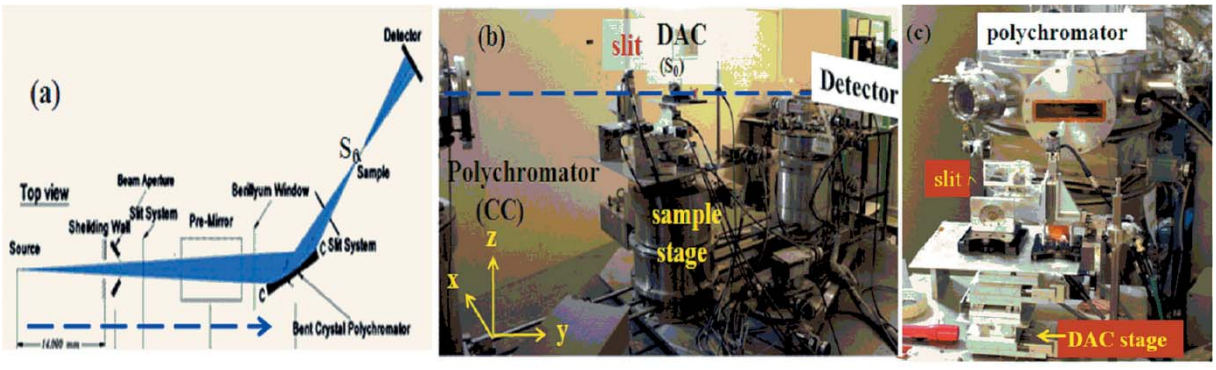

Figure 2
(*a*) Schematic diagram and (*b*) photograph of the BL-8 beamline. The main components are labelled: polychromator (CC), slit, DAC mounted on motorized sample stage at focal spot S_0, position-sensitive detector. Beam direction is depicted by the blue dashed line. The geometry of the experimental configuration is defined with respect to the (*x*, *y*, *z*) axes, described in the text. (*c*) Front view of the polychromator, slit and DAC stage in sequence.

the polychromator surface. Following transmission through the sample, the beam diverges and is recorded on a position-sensitive detector further downstream. The energy–spatial correlation of the beam from the polychromator is converted into an energy–pixel position correlation at the detector. Thus, the whole XAFS spectrum is simultaneously recorded in an acquisition time of ∼300 ms. The suitability of an energy-dispersive beamline for DAC-based HPXAFS are (i) a micrometre-sized beam at the sample point, due to focusing optics; (ii) photon intensity $\sim 10^{12}$ photons s^{-1} mm^{-2} (Das *et al.*, 2007) and (iii) the absence of mechanical movement of optical elements during data acquisition, so that the initial alignment remains valid for the entire experiment. The beamline has been significantly upgraded for HPXAFS experiments by: (i) mounting a precise motorized five-axis sample stage from Kozhu (Kunz *et al.*, 2005; Smith & Desgreniers, 2009; https://www.kohzuprecision.com/products/positioning-stages); (ii) the development of a program for automated sample stage scanning (Dwivedi *et al.*, 2018); (iii) the addition of a slit (on the motorized stage) for further reduction of beam size; (iv) the inclusion of a sensitive Mythen detector for data collection (https://www.psi.ch/en/detectors/mythen).

The Nb *K*-edge (18.995keV) was selected for HPXAFS primarily to minimize absorption within the 4 mm-thick diamond windows of our DAC. Nb-based materials are of scientific interest as a key trace element in Earth's evolutionary process (Sanloup *et al.*, 2018) and multi-functionalities *e.g.* superconductors (Abud *et al.*, 2017; Shimizu *et al.*, 2018; Ishizu & Kitagawa, 2019; Guo *et al.*, 2019), structural material (Jansto & Marquis, 2013), medical implants (Xu *et al.*, 2013), catalysts (Ichikuni *et al.*, 2016; Pinto *et al.*, 2018), and electronic (Alharthi *et al.*, 2018) and photonic devices (Sahiner *et al.*, 2016). Multivalent states of Nb (Nb^{+2}/Nb^{+4}/Nb^{+5}) present the scope for transition between oxidation states and structure under variable external conditions, including pressure (Filonenko & Zibrov, 2001; Tamura, 1972). As a result, a wide range of high-pressure induced problems could be defined for Nb-based materials, *e.g.* understanding high-pressure behavior of structural materials (Kulagin *et al.*, 2018; Nikulina, 2003) or pressure-tuned T_C of superconductors (Edalati *et al.*, 2014; Guo *et al.*, 2017; Ezenwa & Secco, 2017; Ponyatovsky *et al.*, 2009). Thus, the choice of the Nb *K*-edge for HPXAFS is scientifically rich and promising. However, we selected a standard compound Nb_2O_5 (Nb^{+5}) for our first HPXAFS experiments, for its known pressure-induced structural transition (monoclinic → orthorhomic) (Guan *et al.*, 2019; Filonenko & Zibrov, 2001; Tamura, 1972; Zibrov *et al.*, 1998) and reported reference XAFS spectra under ambient and high-pressure conditions (Fig. S3 of Guan *et al.*, 2019; http://ixs.iit.edu/database/data/Farrel_Lytle_data/RAW/Nb/index.html). Our challenge was to reproduce XAFS/HPXAFS spectra for Nb_2O_5 through good quality data and obtain a realistic estimate of the feasibility of HPXAFS experiments at BL-8.

We have designed a (non-trivial) beamline alignment method for maximizing photon statistics at the sample position and minimizing systematic errors. A detailed alignment procedure is described in the paper, with rationalization for every step. We have demonstrated that, in the absence of advanced focusing optics, XANES data of reasonable quality can be generated with three key strategies: (i) selection of a high X-ray energy edge (14–20 keV); (ii) truncation of the smallest achievable spot size (∼277 µm in our case) to target size (∼120 µm in our case) with a slit; optimization of the horizontal slit position, such that the desired energy band ($E_0^{Nb} \pm 100$ eV in our case) is passed and the rest of the beam footprint on the DAC is blocked; (iii) optimization of the DAC orientation for minimum glitches. With these strategies, we successfully reproduced the reported XANES spectra of Nb_2O_5 under pressure (P = 0–16.9 GPa) (http://ixs.iit.edu/database/data/Farrel_Lytle_data/RAW/Nb/index.html; Fig. S3 of Guan *et al.*, 2019). HPXANES for Nb_2O_5 demonstrates a significant pressure-dependent increase in intensity of the post-edge first derivative peak, consistent with the reported HPXANES (Fig. S3 of Guan *et al.*, 2019), and represents improved ordering due to the monoclinic → orthorhombic transition (Guan *et al.*, 2019; Filonenko & Zibrov, 2001; Tamura, 1972; Zibrov *et al.*, 1998). This demonstrates a successful initiation of HPXANES at Indus-2; the prospect of improving data quality over the EXAFS regime is addressed. This work should inspire and guide future HPXAFS experiments, with comparable infrastructure as ours.

2. Experimental details

2.1. DAC description

Standard symmetrical DACs from SYNTEK (http://www.syntek.co.jp) were used, with diamond anvils of thickness 2 mm each and culet size 300 µm. The sample chamber is a hole of diameter 120 µm drilled at the center of a pre-indented tungsten gasket of thickness 35–40 µm. Powdered Nb_2O_5 with a 10 µm ruby chip was loaded in the hole for HPXAFS measurements. No transmitting medium was loaded so that the sample remains uniformly distributed in the hole. In the absence of a transmitting medium, the hole (∼120 µm) was completely filled with the sample in order to resist collapse at increased pressures. Thus, the gasket hole size defined the sample size of ∼120 µm in our case and target beam size of ≤120 µm for alignment. Pressure was measured by the ruby fluorescence method (King Jr & Prewitt, 1980).

2.2. XAFS alignment

A schematic of the beamline configuration of BL-8 is depicted in Fig. 2(*a*). Parameters of the optical elements are listed in Table 1. The polychromator chamber is mounted on the θ-axis of the goniometer and the (slit, sample, position-sensitive detector) stages on the 2θ arm. A photograph of the (post-polychromator) real beamline is presented in Fig. 2(*b*); a magnified image of the polychromator, slit and sample stages sequence is presented in Fig. 2(*c*). The geometry (xyz) of this configuration may be defined with respect to the beam axis [Fig. 2(*b*)], where (i) the positive y-axis runs parallel to the beam direction; and (ii) z and x are the vertical and horizontal

Table 1
Specifications of optical elements at BL-8.

Optical element	Parameter
Source size (theoretical)	0.8 mm × 0.8 mm
Harmonic rejection pre-mirror (M)	
Coating	Rhodium
Radius	1.32 km (fixed)
Angle	0.2° (fixed)
Distance from source	18000 mm
Focusing direction	Vertical
Bent crystal polychromator (CC)	
Material	Si(111)
Radius	0.028–0.265 km
Bragg angle	5.67°–23.29°
Energy	5–20 keV
Energy band	300–1000 eV
Focusing direction	Horizontal
Focus distance	570–1404 mm

axes, respectively, in the plane normal to the beam. The focal point of the beam along the beam axis (y) is defined as S_0 [Fig. 2(*a*)–2(*b*)]. Beamline alignment proceeds in four main stages: (i) tuning the Si(111) polychromator at the Nb *K*-edge and bending it to generate a focused beam at S_0; (ii) truncating the spot with a slit as the focused spot size is larger than the gasket hole; (iii) centering the DAC at S_0; (iv) HPXAFS data collection on Nb_2O_5, loaded inside the DAC. A position-sensitive (2048 × 2048) pixel CCD detector (https://andor.oxinst.com/products/idus-spectroscopy-cameras; model No: DW436F0) and photodiode detector (https://optodiode.com/products-photodiodes.html) were employed for initial alignment; a position-sensitive Mythen detector (https://www.psi.ch/en/detectors/mythen) was employed for final data collection.

2.3. Tuning the polychromator at the Nb *K*-edge (E_0 = 18.988 keV) and focusing the beam

2.3.1. Focusing of the beam. The geometrical parameters for the Si(111) crystal alignment were pre-calculated for different X-ray energies (Das *et al.*, 1999). The crystal was set at the Bragg angle (θ_B = 5.97°) for the Nb *K*-edge (E_0^{Nb} = 18.995 keV). [Higher harmonics are rejected by a Rh pre-mirror, Fig. 2(*a*).] Success of the HPXAFS experiment largely rests on minimizing the focal spot size at S_0. However, in the present phase of commissioning, the crystal was bent in fail-safe mode to avoid breaking. The radius of curvature at the crystal pole was calculated to be R = 24.3 m to deliver the energy band ΔE = 1 keV, following the equation

$$\Delta E = E_0^{Nb}\, l \cot\theta_B \left(\frac{1}{R} - \frac{\sin\theta_B}{p}\right),$$

where p is the distance from the source [= 20 m (fixed)] and l is the length of the crystal illuminated by the beam (Lee *et al.*, 1994; Das *et al.*, 1999). The distance of the focal point (S_0) from the crystal was pre-calculated to be q = 1.335 m from the equation

$$\frac{1}{\sin\theta_B} = \frac{R}{2}\left(\frac{1}{p} + \frac{1}{q}\right)$$

(Das *et al.*, 1999). A CCD detector was accordingly positioned at S_0 to image the diffracted beam during the focusing exercise. The four-point crystal bending mechanism was employed to generate a focused beam (Das *et al.*, 2004). The rectangular crystal, of varying width along its length, is held in position by two fixed inner rods and pushed by two motorized external moving rods. The focusing scheme is outlined in Fig. 3(*a*). A motorized slit of width 50 µm is temporarily inserted in front of the crystal and positioned at three discrete points of the beam in succession, namely left extreme (L), center (C) and right extreme (R). The corresponding CCD pixels of the diffracted beam (P_L, P_C, P_R) were identified and used as markers during the focusing exercise. The principle of the focusing exercise was to alternatively bring the left end (P_L) and right end (P_R) of the beam towards the center (P_C). The two external rods of the crystal bender were moved to this effect until (P_L, P_C, P_R) converged at a point. This point is defined as the focal point S_0. An image of the focused beam on

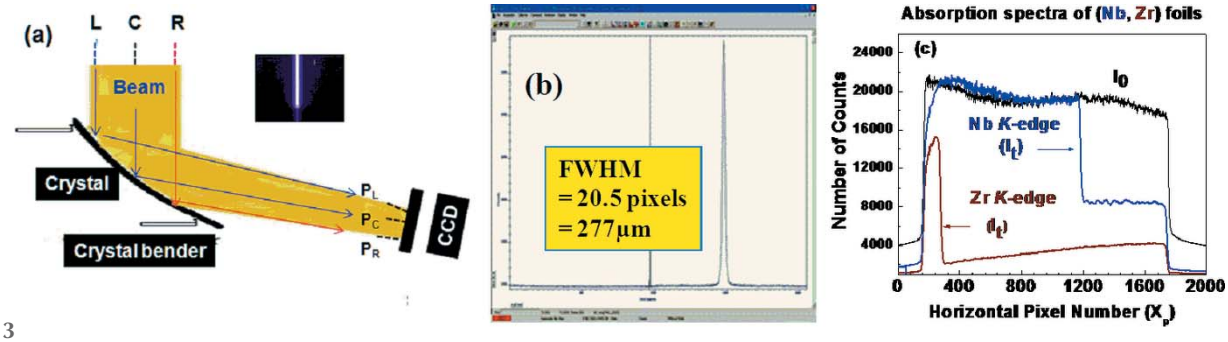

Figure 3
(*a*) Scheme of horizontal beam focusing with crystal bender. The CCD is positioned at a pre-calculated focal distance. Points L, C and R of the beam correspond to points P_L, P_C and P_R on the CCD. Bender motors are moved until P_L, P_C and P_R converge to one point on the CCD, defined as the focal point (S_0). Shown in the inset is the beam profile on the CCD at S_0 [The vertical streak is formed because of readout electronics. Potentials are sequenced simultaneously for readout, so as to shift X-ray induced charges towards the output register row. As potential wells are nearly/completely filled due to high beam intensity, a shadow is formed while transferring this charge. In principle, this effect could be removed by a large thick X-ray absorber in front of the CCD.] (*b*) Horizontal profile of the beam extracted on the CCD. The FWHM of the profile, calculated by CCD software, is 20.5 pixels. (*c*) Absorption spectra I_t of (Nb, Zr) foils recorded on the CCD. Incident beam spectra I_0 are shown for reference. Large dips in absorption represent (Zr, Nb) *K*-edges: X_p = 280 (Zr), X_p= 1177 (Nb).

the CCD at S_0 is displayed in the inset of Fig. 3(*a*); the horizontal profile of the beam is extracted and presented in Fig. 3(*b*). Since each CCD pixel size is 13.5 µm (Das *et al.*, 1999), the horizontal beam size at S_0 was calculated from the FWHM of this profile: $\sigma_H = 277$ µm. The spot size is significantly larger than our target size (120 µm) and design value (Das *et al.*, 1999; Ramanan *et al.*, 2012*a*,*b*), which could be due to an enlarged source size or scattering from optical elements.

2.3.2. Energy calibration. For spectral analysis, the CCD detector was positioned 1.17 m behind S_0. The energy band (ΔE = 1 keV) from the crystal covered both Zr and Nb *K*-edges (E_0^{Zr} = 18.008 keV; E_0^{Nb} = 18.995 keV). Nb and Zr foils were alternately positioned at S_0 and their absorption spectra (I_t) recorded on the CCD [Fig. 3(*c*)]. Pixel numbers [X_p = (280, 1177)] correspond to Nb and Zr *K*-edges in Fig. 3(*c*), from which the pixel resolution was deduced to be 1.1 V pixel^{-1}. This linear conversion factor was preliminarily used to convert *K*-edge spectra on the CCD onto the energy scale (E): $E = E_0^{Nb} + 1.1(X_p - 1177)$. Post-conversion, the XAFS spectrum of the Nb foil is observed to extend from the pre-edge ($E_0^{Nb} - 800$) eV to the post-edge ($E_0^{Nb} + 476$) eV. Post-edge, ΔE = 476 eV corresponds to k_{max} = 11 Å^{-1} ($\Delta E = 3.8k^2$), which is ample for both XANES and EXAFS analysis. Thus, we ensure that an adequate energy band is available for our experiments.

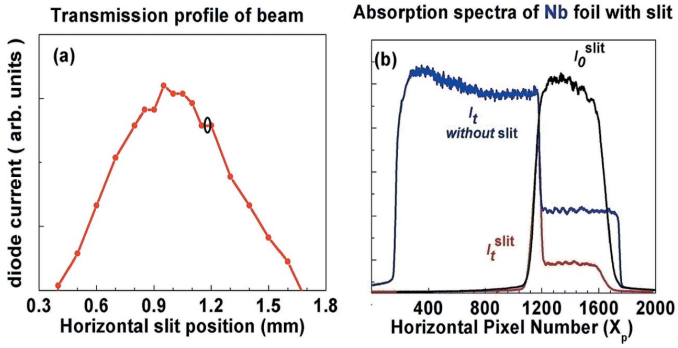

Figure 4
(*a*) Horizontal beam profile of the beam transmitted through a slit of size 3 mm (H) × 1 mm (V). The optical slit position for transmission of the energy band for the Nb *K*-edge XANES spectra is marked by a black circle. (*b*) Incident beam spectra (I_0^{slit}) on the CCD after slit insertion. Pixels $X_p \leq 1065$ are blocked by the slit. Absorption spectra (I_t^{slit}) of the Nb foil are measured in the presence of the slit.

2.4. Reduction of spot size with slit

The beam size at S_0 (277 µm) had to be reduced further towards the target size (120 µm). This could be potentially achieved by bending the polychromator further at the risk of crystal fracture. To avoid crystal fracture, we resorted to an alternate compromised solution. We truncated the beam size with the slit, at the cost of X-ray energy band due to the position–energy correlation. The slit position was thereafter optimized such that E_0^{Nb} and the post-edge region were adequately included in the energy band.

A slit of opening 3 mm (H) × 1 mm (V) was mounted on a motorized stage between the polychromator and S_0. The slit was centered on the beam axis, by scanning in the *xz*-plane (perpendicular to the beam direction) and measuring the transmitted beam intensity with a photodiode, as a function of slit position. The horizontal profile of the beam transmitted through the slit is displayed in Fig. 4(*a*). The slit was temporarily positioned at the maxima of Fig. 4(*a*), which essentially centered it on the beam axis.

The energy profile of the truncated beam was next analyzed on the CCD. To realize this, absorption spectra of the Nb foil were recorded for discrete slit positions within ±600 µm around the maxima. Different segments of the absorption spectra were intercepted for different slit positions. The slit was finally positioned at a +200 µm offset from maxima [marked in Fig. 4(*a*)], where the energy band ($E_0^{Nb} - 100$ eV → $E_0^{Nb} + 200$ eV) passed [shown by I_t^{Nb} in Fig. 4(*b*)]. This covers the entire XANES range and k_{max} = 7 Å^{-1} of the EXAFS regime, which could be sufficient for nearest-neighbor analysis. Intensity was compromised by 6% due to the offset from the maxima position.

The final post-slit focal spot size was estimated from Fig. 4(*b*), by comparing the beam profiles before (I_0) and after slit insertion (I_0^{slit}). It demonstrates a truncation of the beam to 32% of its original size at S_0, which is closer to our target size. Optimization of the slit position sets the step for DAC alignment at S_0. Our improvised utilization of the slit could be adopted as an efficient solution for limited focusing facilities.

2.5. DAC positioning

A blank DAC was mounted on a motorized five-axis stage [Fig. 2(*c*)], controlled through a programmable driver-cum-controller. The *xyz*-axes of the stage were defined with respect to the beam direction, as described earlier [Fig. 2(*b*)]. A drawing of the stage is presented in Fig. 5(*a*) for clarity. From bottom to top [Fig. 5(*a*)], the integrated sample stage consists of (i) a horizontal *X* translation stage (resolution = 1 µm); (ii) a horizontal in-plane (φ) rotation stage (vertical axis of rotation, angular resolution = 0.0002°); (iii) an *xy*-translation stage (resolution = 1 µm); (iv) a *z*-translation stage (resolution = 1 µm). The DAC was secured on the topmost stage by pneumatic lock. The whole sample stage was mounted on a compatible plate fabricated for this purpose.

2.5.1. Translational positioning. A blank DAC was centered on the beam axis, by scanning in the *xz*-plane normal to the beam direction and measuring the transmission profile with a photodiode. The DAC was first coarsely translated onto the beam path with the bottom-most *X* stage (step size ∼200 µm), followed by finer positioning with the topmost *xz*-stage (step size ∼20 µm). Fine scanning in the vertical (*xz*) plane was automated by developing the Labview-based 2D-scanning software program (Dwivedi *et al.*, 2018). The electronic loop for the program is depicted in Fig. 5(*b*). The DAC position (x_{DAC}, z_{DAC}), corresponding to the centroid of the transmission profile maxima, was finalized. This essentially centered the DAC on the beam axis, in the *xz*-plane perpendicular to the beam direction. The DAC position along the beam direction was next optimized with the *y*-translation stage. The

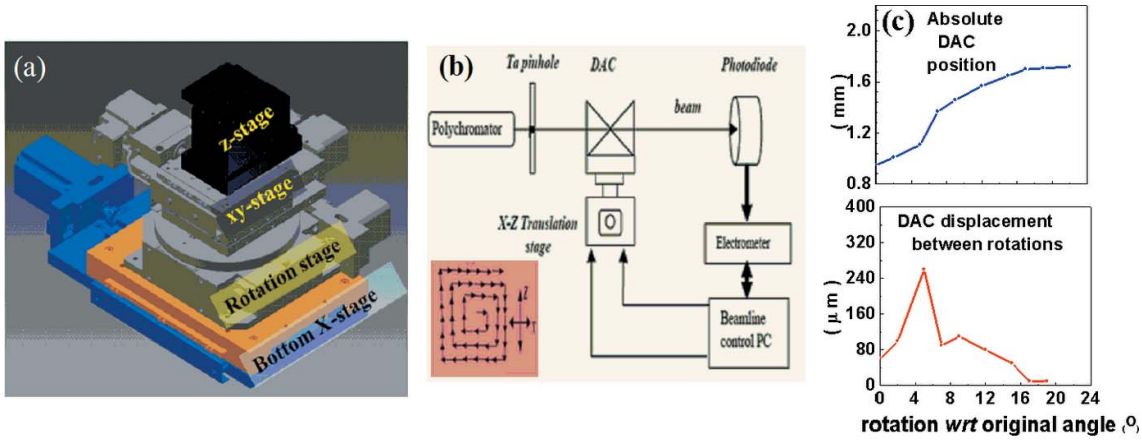

Figure 5
(*a*) Five-axis motorized sample stage. From bottom to top: *X* translation stage, rotation stage, *xy* translation stage and *z*-translation stage [*xyz*-axes are defined with respect to beam direction in Fig. 2(*b*)]. The DAC is mounted on the topmost stage. (*b*) For translational positioning of the DAC, electronic loop for automated *x*–*z* scanning of the DAC. The *x*–*z* scanning algorithm is displayed in the inset on the left. (*c*) For centering the DAC at the center of rotaion of the goniometer, the DAC is rotated. The *x*-position of the DAC (x_{DAC}) as a function of rotation angle is shown at the top. The rotation-induced displacement of the DAC (Δx_{DAC}) as a function of angle is shown at the bottom.

transmitted beam intensity (I_{diode}^{DAC}) is sensitive to the DAC location on the beam axis, due to the divergent geometry of the beam with respect to S_0. As the DAC is translated away from S_0 the gasket intercepts increasing portions of the divergent beam that results in decreasing I_{diode}^{DAC}. The DAC position at S_0 maximizes I_{diode}^{DAC}. Hence, the position (y_{DAC}), corresponding to the centroid of the I_{diode}^{DAC} maxima, was finalized to be on the focal plane.

The energy profile of the beam (I_0^{DAC}) was analyzed on the CCD. Comparison of I_0^{DAC} with I_0^{slit} (in the absence of the DAC) in Fig. 6(*a*) demonstrates the alignment of their centroids (X_p = 1380), reconfirming centering of the DAC on the beam axis. The presence of the DAC clearly modulates the incident beam by (*a*) an 80% reduction in intensity due to absorption within diamond, (*b*) truncating the beam further by 8% with the gasket; and (*c*) the presence of glitches superimposed on the background. Absorption of the Nb foil (I_t^{DAC}) was remeasured by fixing the foil behind the DAC [Fig. 6(*b*)]. From Fig. 6(*b*), it is observed that although I_t^{DAC} fluctuations follow glitches of I_0^{DAC}, their ratio (I_0^{DAC}/I_t^{DAC}) is not properly normalized. As a result, the normalized absorption spectrum, in the presence of the DAC [$\ln(I_0^{DAC}/I_t^{DAC})$], is significantly distorted from the spectra in the absence of the DAC [$\ln(I_0^{slit}/I_t^{slit})$] [Fig. 6(*c*)]. Realizing that this problem arises due to poor counting statistics, we replaced the CCD by a sensitive Mythen detector (https://www.psi.ch/en/detectors/mythen). Mythen is a 1D detector, working in single photon counting mode with advantages of low noise, high dynamic range, spatial resolution, parallel acquisition and fast readout rate (up to 1 kHz). Incident (I_0) and absorption (I_t) spectra of the (Nb, Zr) foils were re-measured with the Mythen for reference (Fig. 7).

2.5.2. Optimization of DAC orientation. The purpose of the rotation stage is for the identification of optimal DAC orientations (φ) that generate the least number of glitches. This pre-requires matching the DAC center (x_{DAC}, y_{DAC}) with

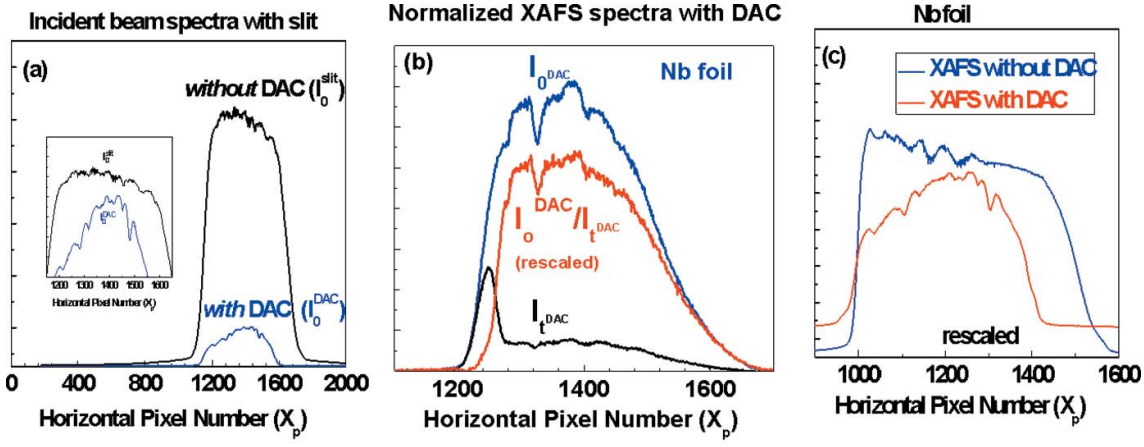

Figure 6
Incident beam post-slit: without DAC (I_0^{slit}) and with DAC (I_0^{DAC}). Rescaled (I_0^{slit}, I_0^{DAC}) are compared in the inset. I_0^{DAC} demonstrates the significant presence of glitches. (*b*) Incident (I_0^{DAC}), absorption (I_t^{DAC}) and (rescaled) normalized absorption spectra (I_0^{DAC}/I_t^{DAC}) for Nb foil in the presence of DACs. (*c*) Comparison of normalized absorption spectra for Nb foil, in the absence and presence of the DAC.

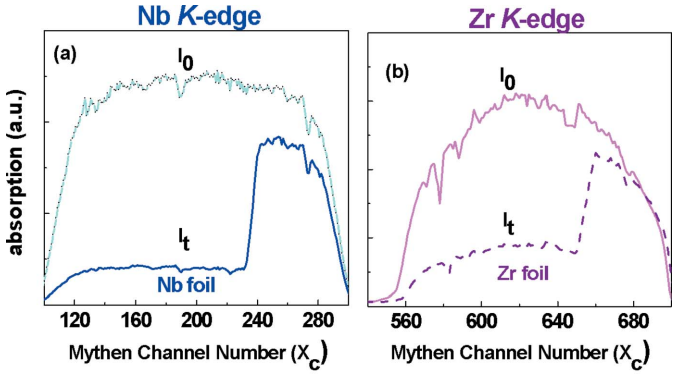

Figure 7
Incident beam spectra (I_0) and absorption spectra (I_t) of (*a*) Nb and (*b*) Zr foils, measured using the Mythen detector.

the center of rotation (x_0, y_0) of the goniometer, so that the DAC is locked at the maximum position for all orientations. Since the maxima of the beam profile at S_0 extend over a plateau of ∼60 µm [Fig. 3(*b*)], the DAC position is ambiguous to this extent. This leaves room for ambiguity in the relative positions of the DAC and center of rotation. We centered the DAC at (x_0, y_0), following the method of Kunz and Smith (Kunz *et al.*, 2005; Smith & Desgreniers, 2009). The method involved DAC rotation in steps of $\Delta\varphi_i$; following each rotation, the transmission profile was measured by scanning the DAC in the *x*-direction. Rotation entailed displacement of transmission maxima, so that the DAC had to be repositioned following each rotation. The DAC position $(x_{DAC})_i$, as a function of rotation angle, is plotted in Fig. 5(*c*). The rotation-induced DAC displacement $\Delta(x_{DAC})_i$ is also plotted, as a function of angle. Fig. 5(*c*) clearly demonstrates tapering of the DAC displacement with progressive rotation. The exercise was reiterated until the displacement reduced to ∼10 µm beyond 17°, suggesting that the DAC and rotation center are in close proximity. Displacements for $\Delta\varphi = \pm 2°$ with respect to 19° on the plot [Fig. 5(*c*)], namely $\Delta x^{\pm}_{DAC} = 10$ µm, were used to calculate the offset between (x_{DAC}, x_0) and (y_{DAC}, y_0),

$$\Delta x = \frac{\Delta x^{+}_{DAC} + \Delta x^{-}_{DAC}}{2[1 - \cos(2°)]} = 16\ \mu\text{m},$$

$$\Delta y = \frac{\Delta x^{+}_{DAC} - \Delta x^{-}_{DAC}}{2\sin(2°)} = 0\ \mu\text{m}$$

(Smith & Desgreniers, 2009). The relative translation of the DAC by −16 µm in the *x*-direction places the DAC at the center of the rotation.

Absorption spectra of the blank DAC (I_0^{DAC}) were measured with Mythen, for DAC rotations within $\Delta\varphi = \pm 4°$ about the current position [Fig. 8(*a*); angles are marked 265°–275°]; positions of glitches shift with varying φ. Absorption spectra of Nb foil (I_t^{DAC}) were measured for all orientations by fixing the foil behind the DAC. Reproducibility of the normalized absorption spectra $[\ln(I_0^{DAC}/I_t^{DAC})]$ for different orientations [Fig. 8(*b*)] confirms that glitches in I_0^{DAC} are well normalized for Mythen (unlike the CCD). The orientation (φ = 271°) was finalized for HPXAFS for its minimal glitch content.

Translational $(x_{DAC}, y_{DAC}, z_{DAC})$ and angular (φ) optimization of the DAC sets the stage for HPXAFS data collection.

2.6. HPXAFS data collection

A small ruby sphere was loaded into the corner of the sample chamber of the DAC for pressure calibration with the R1 fluorescence peak position (King Jr & Prewitt, 1980). The ruby-filled DAC was reinstated at the marked position. Following ruby loading, absorption spectra were remeasured for the ruby-filled blank DAC (I_0^{DAC}) and Nb foil (I_t^{DAC}), fixed behind the ruby-filled blank DAC. Normalized absorption spectra $[\ln(I_0^{DAC}/I_t^{DAC})]$ are compared for (i) pre-ruby and (ii) post-ruby loadings [Fig. 8(*c*)]. Their reproducibility within the error bar confirms that spectral intereference from the ruby is negligible. Following DAC alignment, the setup is ready for actual HPXAFS data collection on Nb_2O_5. The purity of monoclinic Nb_2O_5 was pre-confirmed with X-ray diffraction (XRD). (The XRD spectrum is presented in Fig. S1 of the supporting information.) Absorption spectra (I_t^{DAC}) of Nb_2O_5 powder were measured (i) behind the DAC (uniformly pasted on tape) and (ii) inside the ruby-loaded DAC. The absorption spectra were normalized by I_0^{DAC} corresponding to the ruby-filled DAC. Fig. 9(*a*) compares normalized absorption spectra $[\ln(I_0^{DAC}/I_t^{DAC}]$ of Nb_2O_5, measured (i) outside and (ii) inside the DAC at ambient pressure. It is clear that the signal-to-noise ratio is weakened for Nb_2O_5 inside the DAC due to the smaller sample amount; as a result, glitches become prominent in the EXAFS region. Nonetheless, XANES features of interest, namely white line and shoulder, are unperturbed between outside and inside the DAC. For each pressure point, the pressure of the

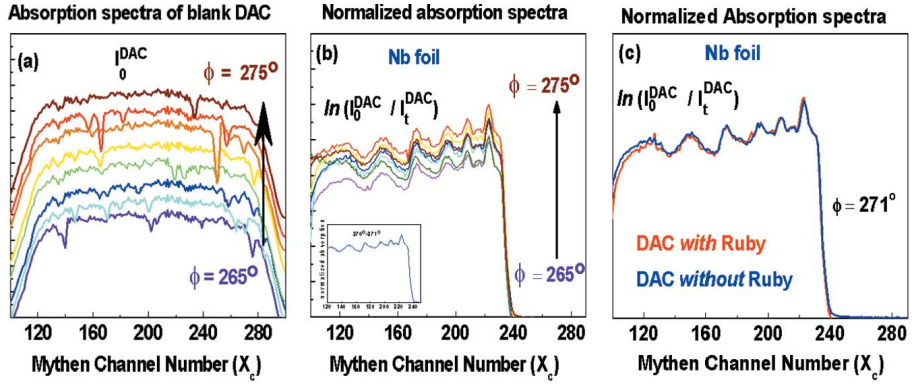

Figure 8
(*a*) Incident I_0^{DAC} and (*b*) normalized absorption $[\ln(I_0^{DAC}/I_t^{DAC})]$ spectra for Nb foil, measured with the Mythen detector for different DAC orientations (φ = 265°–275°). Datasets for different φ are offset for clarity. The reproducibility of the XAFS spectra for φ = 270°–271° is shown in the inset of (*b*). (*c*) Comparison of normalized absorption spectra $[\ln(I_0^{DAC}/I_t^{DAC})]$ for Nb foil, without and with a ruby inside the DAC at φ = 271°.

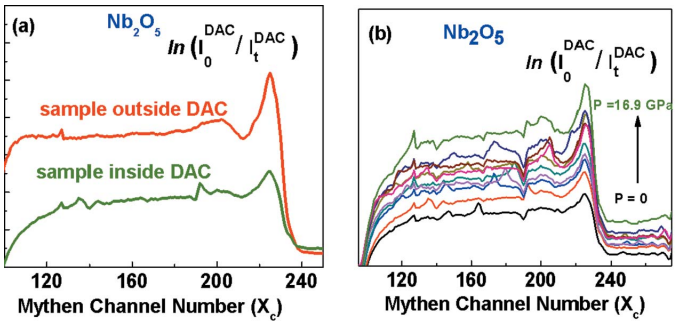

Figure 9
(*a*) Normalized absorption spectra $[\ln(I_0^{DAC}/I_t^{DAC})]$, compared for measurements of Nb_2O_5 powder outside and within the DAC. Datasets are offset for clarity. (*b*) Normalized absorption spectra $[\ln(I_0^{DAC}/I_t^{DAC})]$ for Nb_2O_5 powder loaded inside the DAC, as a function of pressure.

sample-loaded DAC was increased and its value determined (± 0.2 GPa); the sample-loaded DAC was then reinstated in the beamline for absorption data collection at that pressure point. The data acquisition time was set at 100 s per spectrum. This exercise was reiterated for nine pressure points between $P = 0$ and $P = 16.9$ GPa. Pressure-dependent normalized absorption spectra $[\ln(I_0^{DAC}/I_t^{DAC})]$ for Nb_2O_5 are presented in Fig. 9(*b*). High-pressure absorption spectra demonstrate a significant edge jump despite 80% absorption within the DAC windows. The XANES region of the spectra is clean and analyzable while the EXAFS region is dominated by glitches and noise. This limits the analysis to XANES temporarily.

3. Results and discussions

3.1. Data calibration

At this stage, Nb *K*-edge data of BL-8 were converted from Mythen channel number (X_c) to energy scale (E) and from relative (μ_c) to absolute absorption scale (μ), by comparing with reference spectra for Nb_2O_5 (http://ixs.iit.edu/database/data/Farrel_Lytle_data/RAW/Nb/index.html). As mentioned in the previous section, we focus our analysis on the XANES portion of the spectra. Derivative XANES spectra offer better resolution and were used for calibration [Figs. 10(*a*) and 10(*b*)]. The derivative of the XANES spectrum in pixel units [Fig. 10(*a*)] was generated for Nb_2O_5 outside the DAC, from the data of Fig. 9(*a*). (This derivative dataset is referred to as the BL-8 data henceforth.) Derivative spectra for (i) the reference (international) Nb_2O_5 on energy (E) scale and (ii) the BL-8 dataset on the (X_c) scale are presented in Figs. 10(*a*) and 10(*b*). [Note that X_c of Fig. 10(*b*) has been offset with respect to Fig. 9(*a*) for convenience of calculation.] Both spectra exhibit common maxima and minima with coordinates $(E, \mu)_i$ and $(X_c, \mu_c)_i$, respectively. One-to-one correspondence was identified between coordinates (E, X_c) and (μ, μ_c) of the two spectra. These correlations are plotted in Fig. 10(*c*) (E, X_c) and 10(*d*) (μ, μ_c), respectively. Each of these plots in Fig. 10(*c*) and 10(*d*) was fitted (adequately) with a second-order polynomial: $E = 18940.4 + 2.574X_c + 0.0036X_c^2$; $\mu = 0.0043 + 0.2339\mu_c + 0.491\mu_c^2$ (Ruffoni & Pettifer, 2006). These conversion formulae were henceforth applied to each data point $(X_c, \mu_c)_i$ of the BL-8 dataset [Fig. 10(*b*)] to generate

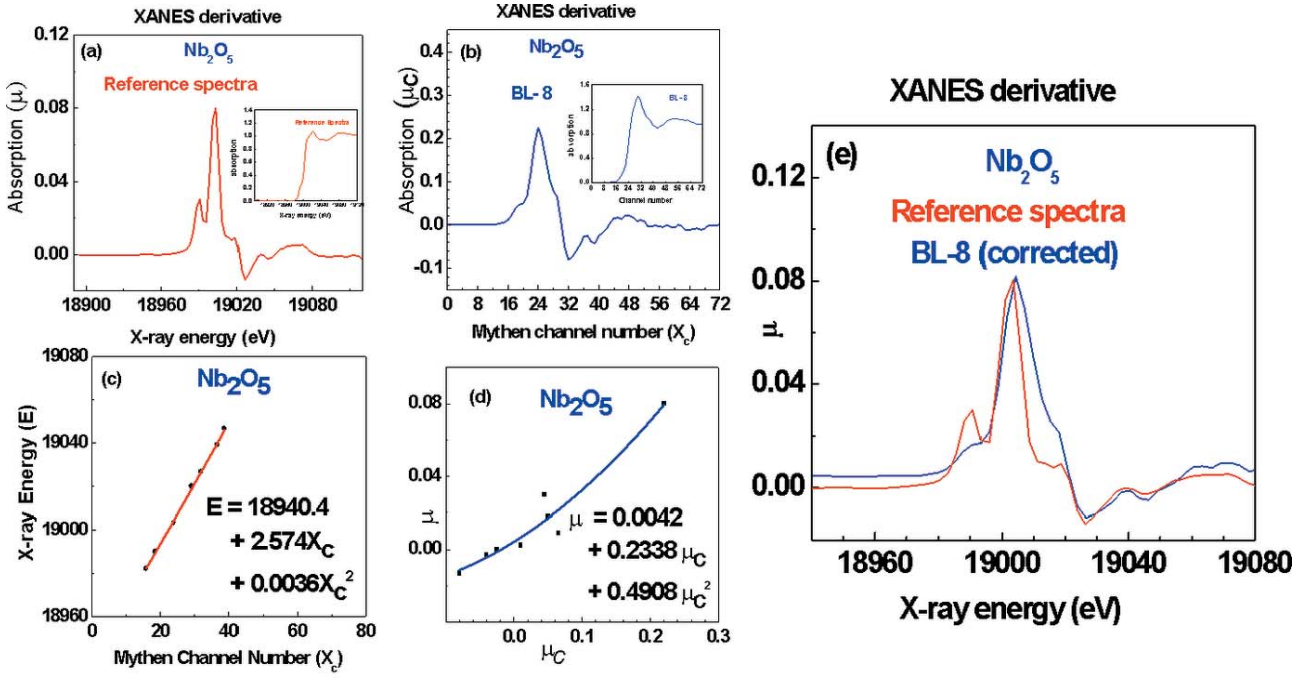

Figure 10
XANES derivatives for Nb_2O_5. (*a*) Reference spectra (μ) on the energy (E) scale and (*b*) absorption spectra (μ) in channel number units (N_c), for the sample measured outside the DAC at BL-8. Original XANES spectra are shown in the respective insets. Correlations obtained from the two spectra (*c*) (E, X_p) and (*d*) absorption amplitudes (μ, μ_c). Best fit equations for the respective correlations are displayed in (*c*) and (*d*). (*e*) XANES derivative spectra generated from BL-8 data, by converting $(X_c \rightarrow E)$ and $(\mu_c \rightarrow \mu)$.

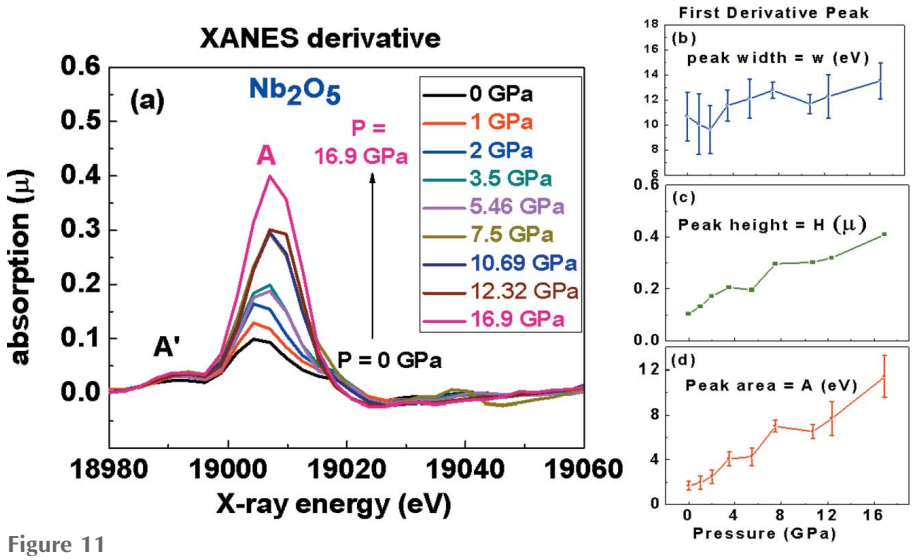

Figure 11
XANES derivative spectra for Nb_2O_5 under different pressures. First peak of the XANES spectra: (*b*) width, (*c*) height and (*d*) area, as a function of pressure.

the corresponding $(E, \mu)_i$. This completes the conversion from X_c to E and from μ_c to μ for the BL-8 data. Converted BL-8 spectra and reference spectra are compared in Fig. 10(*d*); a good match of features and calibration for both (E, μ) axes is confirmed. The only difference between the BL-8 dataset and reference spectra is broadening of the former due to poor resolution of dispersive optics (Flank *et al.*, 1983; Ruffoni & Pettifer, 2006). [In principle, the reference spectra can be convolved with instrumental weight functions to reproduce the BL-8 spectra (Ruffoni & Pettifer, 2006).] These $(X_c, \mu_c) \rightarrow (E, \mu)$ conversion formulae are valid for subsequent XANES spectra due to the advantage of static optics. Datasets of Fig. 9(*b*) were henceforth corrected by applying these conversion formulae; corrected derivatives are presented in Fig. 11(*a*).

3.2. HPXANES analysis

HPXANES derivative spectra [Fig. 11(*a*)] exhibit (i) a small secondary peak (A') at 18992 eV and (ii) a main peak (A) at 19005 eV, corresponding to the pre-edge and main rising edge of the XAFS spectra, respectively. [Pre-edge peak (A') is too small for unambiguous quantitative analysis.] We focused our analysis on the main peak (A), which demonstrates a conspicuous increase of intensity between P = 0 and P = 16.9 GPa. The peak lineshape, for each pressure point, was fitted with a Lorentzian function,

$$y = y_0 + \frac{2A}{\pi}\,\frac{w}{4(E - E_0)^2 + w^2},$$

to derive the centroid (E_0), width (w), amplitude (H) and area (A = 1.57wH). The centroid ($E_0 \simeq$ 19005 eV represents the edge position of the XAFS spectra. Pressure-dependent variations of (w, H, A) are displayed in Figs. 11(*b*)–11(*d*). Error bars reflect possible deviations from a Lorentzian shape. The peak width (w), which represents the energy bandwidth, is approximately (within error bars) preserved under pressure [Fig. 11(*b*)]. On the other hand, the amplitude (H), representing the absorption edge gradient, demonstrates a significant (×4) increase between P = 0 and P = 16.9 GPa [Fig. 11(*c*)]. Escalation of the absorption gradient is consistent with the development of increasingly pronounced white line (Brown *et al.*, 1977; Lu *et al.*, 1992), which is a signature of improved order. The pressure-dependent increase of the white line is consistent with the reported HPXANES spectra for Nb_2O_5 (Fig. S3 of Guan *et al.*, 2019). Demonstration of the improved order is consistent with the pressure-induced monoclinic to orthorhombic transition (Guan *et al.*, 2019; Filonenko & Zibrov, 2001; Tamura, 1972; Zibrov *et al.*, 1998). Thus, Nb *K*-edge HPXANES at BL-8 reproduces the reported high-pressure transition of Nb_2O_5.

3.3. Scope of improvement

This meets our target of generating analyzable and reliable XAFS spectra, at least in the XANES region. Direct structural determination with EXAFS would have reinforced our success, which we plan to accommodate in the next stage of the upgrade at BL-8. The target is to strengthen signal statistics by improving (i) horizontal focusing with further bending of the polychromator and (ii) vertical focusing with a bendable elliptic mirror purchased from SESO (http://seso.com/new-services/x-rays/x-ray-mirrors/). The mirror was preliminarily installed in the first phase of commissioning (Ramanan *et al.*, 2015) and has been motorized recently for precise alignment in the future. With these ammendments, we hope to extend the scope of HPXAFS at BL-8.

4. Conclusion

In this work, we reported the initiation of diamond anvil cell based high-pressure XANES experiments at the energy-dispersive XAFS beamline BL-8 of the Indus-2 synchrotron facility, India. In the framework of limited photon statistics due to the bending-magnet source and 4 mm-thick diamond windows of the DAC, we selected the Nb *K*-edge to minimize absorption within the diamond and we designed an alignment method to maximize photon flux at the sample position. In the absence of advanced focusing optics, we generated a DAC-compatible beam spot size (∼120 μm) at the Nb *K*-edge with the combination of polychromator-induced bending and further truncation of the spot size with a slit. The slit position was judiciously optimized to select the desired X-ray energy range from the position–energy correlation. A rigorous method, based on X-ray transmission through the DAC, was

adopted to precisely center the DAC at the focus and optimize its orientation for minimum glitches. With these strategies, we generated good quality Nb *K*-edge XANES spectra for Nb_2O_5 under high pressure (0–16.9 GPa). We converted the data from detector channel number into energy scale, following a prescribed calibration alogrithm. Our results reproduced reported XANES spectra for Nb_2O_5 under ambient and high-pressure conditions. Good data quality permitted quantitative analysis of HPXANES derivative spectra that established a pressure-induced significant (×4) increase in ordering, consistent with the reported monoclinic to orthorhombic transition. This demonstrates a successful initiation and feasibility of high-pressure XANES experiments at BL-8, Indus-2. Our success and roadmap for extending good data quality into the EXAFS regime should inspire and guide future HPXAFS experiments with comparable infrastructure as ours.

Acknowledgements

We thank Dr S. M. Sharma, (ex) Head, High Pressure and Synchrotron Radiation Physics Division, Bhabha Atomic Research Centre (India), for initiating us into this project. We thank Dr Srihari Velaga, High Pressure and Synchrotron Radiation Physics Division, Bhabha Atomic Research Centre (India), for measuring XRD of Nb_2O_5 at BL-11, Indus-2, and Dr Ashwini Poswal, Atomic and Molecular Physics Division, Bhabha Atomic Research Centre (India), for fruitful suggestions.

References

Abud, F., Correa, L. E., Souza Filho, I. R., Machado, A. J. S., Torikachvili, M. S. & Jardim, R. F. (2017). *Phys. Rev. Mater.* **1**, 044803.

Alharthi, F. A., Cheng, F., Verrelli, E., Kemp, N. T., Lee, A. F., Isaacs, M. A., O'Neill, M. & Kelly, S. M. (2018). *J. Mater. Chem. C.* **6**, 1038–1047.

Andrault, D., Peryronneau, J., Farges, F. & Itié, J. P. (1995). *Physica B*, **208–209**, 327–329.

Aquilanti, G., Trapananti, A., Karandikar, A., Kantor, I., Marini, C., Mathon, O., Pascarelli, S. & Boehler, R. (2015). *Proc. Natl Acad. Sci. USA*, **112**, 12042–12045.

Bare, S., Kelly, S. D., Ravel, B., Greenlay, N., King, L. & Mickelson, G. E. (2010). *Phys. Chem. Chem. Phys.* **12**, 7702–7711.

Bassett, W. A., Anderson, A. J., Mayanovic, R. A. & Chou, I. (2000). *Chem. Geol.* **167**, 3–10.

Bastea, M., Mitchell, A. C. & Nellis, W. J. (2001). *Phys. Rev. Lett.* **86**, 3108–3111.

Baudelet, F., Kong, Q., Nataf, L., Cafun, J. D., Congeduti, A., Monza, A., Chagnot, S. & Itié, J. P. (2011). *High. Press. Res.* **31**, 136–139.

Bhattacharyya, D., Poswal, A. K., Jha, S. N., Sangeeta & Sabharwal, S. C. (2009). *Nucl. Instrum. Methods Phys. Res. A*, **609**, 286–293.

Boccato, S., Torchio, R., Kantor, I., Morard, G., Anzellini, S., Giampaoli, R., Briggs, R., Smareglia, A., Irifune, T. & Pascarelli, S. (2017). *J. Geophys. Res. Solid Earth*, **122**, 9921–9930.

Boehler, R. (2006). *Rev. Sci. Instrum.* **77**, 115103.

Brown, M., Peierls, R. E. & Stern, E. A. (1977). *Phys. Rev. B*, **15**, 738–744.

Chen, Y., Fulton, J. L. & Partenheimer, W. (2005). *J. Am. Chem. Soc.* **127**, 14085–14093.

Dadashev, A., Pasternak, M. P., Rozenberg, G. K. & Taylor, R. D. (2001). *Rev. Sci. Instrum.* **72**, 2633–2637.

Das, N. C. *et al.* (1999). BARC Report BARC/1999/E035. Bhabha Atomic Research Centre, Mumbai, India.

Das, N. C. *et al.* (2007). BARC Report BARC/2007/E001. Bhabha Atomic Research Centre, Mumbai, India.

Das, N. C., Jha, S. N., Bhattacharyya, D., Poswal, A. K., Sinha, A. K. & Mishra, V. K. (2004). *Sadhana*, **29**, 545–557.

Ding, Y., Haskel, D., Tseng, Y. C., Kaneshita, E., van Veenendaal, M., Mitchell, J. F., Sinogeikin, S. V., Prakapenka, V. & Mao, H. K. (2009). *Phys. Rev. Lett.* **102**, 237201.

Doudna, M., Bertino, M. F., Blum, F. D., Tokuhiro, A. T., Lahiri-Dey, D., Chattopadhyay, S. & Terry, J. (2003). *J. Phys. Chem. B*, **107**, 2966–2970.

Dwivedi, A. *et al.* (2018). *National Conference on Optics Photonics and Synchrotron Radiation for Technological Applications (OPSR-2018)*, 29 April–2 May 2018, Indore, India.

Edalati, K., Daio, T., Lee, S., Horita, Z., Nishizaki, T., Akune, T., Nojima, T. & Sasaki, T. (2014). *Acta Mater.* **80**, 149–158.

Eremets, M. I. (1996). *High-Pressure Experimental Methods.* Oxford University Press.

Ezenwa, I. C. & Secco, R. A. (2017). *J. Appl. Phys.* **121**, 225903.

Filonenko, V. P. & Zibrov, I. P. (2001). *Inorg. Mater.* **37**, 953–959.

Flank, A. M., Fontaine, A., Jucha, A., Lemonnier, M., Raoux, D. & Williams, C. (1983). *Nucl. Instrum. Methods Phys. Res.* **208**, 651–654.

Garg, N. (2017). *Curr. Sci.* **112**, 1430–1443.

Guan, Z., Li, Q., Zhang, H., Shen, P., Zheng, L., Chu, S., Park, C., Hong, X., Liu, R., Wang, P., Liu, B. & Shen, G. (2019). *J. Phys. Condens. Matter*, **31**, 105401.

Guo, J., Lin, G., Cai, S., Xi, C., Zhang, C., Sun, W., Wang, Q., Yang, K., Li, A., Wu, Q., Zhang, Y., Xiang, T., Cava, R. J. & Sun, L. (2019). *Adv. Mater.* **31**, 1807240.

Guo, J., Wang, H., von Rohr, F., Wang, Z., Cai, S., Zhou, Y., Yang, K., Li, A., Jiang, S., Wu, Q., Cava, R. J. & Sun, L. (2017). *Proc. Natl Acad. Sci. USA*, **114**, 13144–13147.

Haskel, D., Fabbris, G., Souza-Neto, N. M., van Veenendaal, M., Shen, G., Smith, A. E. & Subramanian, M. A. (2011). *Phys. Rev. B*, **84**, 100403.

Haskel, D., Tseng, Y. C., Lang, J. C. & Sinogeikin, S. (2007). *Rev. Sci. Instrum.* **78**, 083904.

Haskel, D., Stern, E. A., Polinger, V. & Dogan, F. (1999). *J. Synchrotron Rad.* **6**, 758–760.

Hemley, R. J. (2000). *Annu. Rev. Phys. Chem.* **51**, 763–800.

Hong, X., Newville, M., Prakapenka, V. B., Rivers, M. L. & Sutton, S. R. (2009). *Rev. Sci. Instrum.* **80**, 073908.

Hong, X., Newville, M. & Duffy, T. S. (2013). *J. Phys. Conf. Ser.* **430**, 012120.

Ichikuni, N., Yanagase, F., Mitsuhara, K., Hara, T. & Shimazu, S. (2016). *J. Phys. Conf. Ser.* **712**, 012060.

Impellitteri, C. A., Evans, O. & Ravel, B. (2007). *J. Environ. Monit.* **9**, 358–365.

Ishimatsu, N., Matsumoto, K., Maruyama, H., Kawamura, N., Mizumaki, M., Sumiya, H. & Irifune, T. (2012). *J. Synchrotron Rad.* **19**, 768–772.

Ishizu, N. & Kitagawa, J. (2019). *Results Phys.* **13**, 102275.

Itie, J. P., Polian, A., Calas, G., Petiau, J., Fontaine, A. & Tolentino, H. (1989). *Phys. Rev. Lett.* **63**, 398–401.

Jansto, S. G. & Marquis, F. (2013). Editors. *Proceedings of the 8th Pacific Rim International Congress on Advanced Materials and Processing*, pp. 19–26. Cham: Springer.

Joseph, B., Torchio, R., Benndorf, C., Irifune, T., Shinmei, T., Pöttgen, R. & Zerr, A. (2017). *Phys. Chem. Chem. Phys.* **19**, 17526–17530.

Kantor, I., Marini, C., Mathon, O. & Pascarelli, S. (2018). *Rev. Sci. Instrum.* **89**, 013111.

King, H. E. Jr & Prewitt, C. T. (1980). *Rev. Sci. Instrum.* **51**, 1037–1039.

Koningsberger, D. C. & Prins, R. (1988). X-*ray Absorption: Principles, Applications and Techniques of EXAFS, SEXAFS and XANES*. New York: Wiley.
Kulagin, R., Mazilkin, A., Beygelzimer, Y., Savvakin, D., Zverkova, I., Oryshych, D. & Hahn, H. (2018). *Mater. Lett.* **233**, 31–34.
Kulow, A., Witte, S., Beyer, S., Guilherme Buzanich, A., Radtke, M., Reinholz, U., Riesemeier, H. & Streli, C. (2019). *J. Anal. At. Spectrom.* **34**, 239–246.
Kunz, M., MacDowell, A. A., Caldwell, W. A., Cambie, D., Celestre, R. S., Domning, E. E., Duarte, R. M., Gleason, A. E., Glossinger, J. M., Kelez, N., Plate, D. W., Yu, T., Zaug, J. M., Padmore, H. A., Jeanloz, R., Alivisatos, A. P. & Clark, S. M. (2005). *J. Synchrotron Rad.* **12**, 650–658.
Lahiri, D., Bunker, B., Mishra, B., Zhang, Z., Meisel, D., Doudna, C. M., Bertino, M. F., Blum, F. D., Tokuhiro, A. T., Chattopadhyay, S., Shibata, T. & Terry, J. (2005). *J. Appl. Phys.* **97**, 094304.
Lahiri, D., Sharma, S. M., Verma, A. K., Vishwanadh, B., Dey, G. K., Schumacher, G., Scherb, T., Riesemeier, H., Reinholz, U., Radtke, M. & Banerjee, S. (2014). *J. Synchrotron Rad.* **21**, 1296–1304.
Lee, P. L., Beno, M. A., Jennings, G., Ramanathan, M., Knapp, G. S., Huang, K., Bai, J. & Montano, P. A. (1994). *Rev. Sci. Instrum.* **65**, 1–6.
Liu, J., Wang, S., Qie, Y., Zhang, C. & Sun, Q. (2018). *Phys. Rev. Mater.* **2**, 025403.
Liu, X. (2011). *Mod. Inorg. Synth. Chem.*, ch. 5, pp. 97–128. Amsterdam: Elsevier.
Lu, Z. H., Sham, T. K., Vos, M., Bzowski, A., Mitchell, I. V. & Norton, P. R. (1992). *Phys. Rev. B*, **45**, 8811–8814.
Machon, D., Pischedda, V., Le Floch, S. & San-Miguel, A. (2018). *J. Appl. Phys.* **124**, 160902.
Mathon, O., Baudelet, F., Itié, J.-P., Pasternak, S., Polian, A. & Pascarelli, S. (2004). *J. Synchrotron Rad.* **11**, 423–427.
Mathon, O., Beteva, A., Borrel, J., Bugnazet, D., Gatla, S., Hino, R., Kantor, I., Mairs, T., Munoz, M., Pasternak, S., Perrin, F. & Pascarelli, S. (2015). *J. Synchrotron Rad.* **22**, 1548–1554.
McMillan, P. F. (2002). *Nat. Mater.* **1**, 19–25.
McMillan, P. F. (2003). *High. Press. Res.* **23**, 7–22.
Meneghini, C., Cimino, R., Pascarelli, S., Mobilio, S., Raghu, C. & Sarma, D. D. (1997). *Phys. Rev. B*, **56**, 3520–3523.
Misra, N. L., Lahiri, D., Singh Mudher, K. D., Olivi, L. & Sharma, S. M. (2008). *X-ray Spectrom.* **37**, 215–218.
Miyauchi, K., Qiu, J., Shojiya, M., Kawamoto, Y., Kitamura, N., Fukumi, K., Katayama, Y. & Nishihata, Y. (2002). *Solid State Commun.* **124**, 189–193.
Morozova, N. V., Korobeinikov, I. V. & Ovsyannikov, S. V. (2019). *J. Appl. Phys.* **125**, 220901.
Nikulina, A. V. (2003). *Metal Sci. Heat Treat.* **45**, 287–292.
Pantelouris, A., Kueper, G., Hormes, J., Feldmann, C. & Jansen, M. (1995). *J. Am. Chem. Soc.* **117**, 11749–11753.
Parsons, J. G., Aldrich, M. V. & Gardea-Torresdey, J. L. (2011). *Appl. Spectrosc. Rev.* **37**, 187–222.
Pascarelli, S., Mathon, O., Mairs, T., Kantor, I., Agostini, G., Strohm, C., Pasternak, S., Perrin, F., Berruyer, G., Chappelet, P., Clavel, C. & Dominguez, M. C. (2016). *J. Synchrotron Rad.* **23**, 353–368.
Pascarelli, S., Mathon, O., Muñoz, M., Mairs, T. & Susini, J. (2006). *J. Synchrotron Rad.* **13**, 351–358.
Pascarelli, S. & Mathon, O. (2010). *Phys. Chem. Chem. Phys.* **12**, 5535–5546.
Pascarelli, S., Mathon, O. & Aquilanti, G. (2004). *J. Alloys Compd.* **362**, 33–40.
Pinto, M. B., Soares, A. L. Jr, Quintão, M. C., Duarte, H. A. & De Abreu, H. A. (2018). *J. Phys. Chem. C*, **122**, 6618–6628.
Ponyatovsky, E. G., Bashkin, I. O., Tissen, V. G. & Nefedova, M. V. (2009). *Phys. Solid State*, **51**, 1785–1788.
Ramanan, N. *et al.* (2012*a*). BARC Report BARC/2012/E/009. Bhabha Atomic Research Centre, Mumbai, India.
Ramanan, N., Kumar, A., Rajput, P., Thankarajan, K., Bhattacharyya, D., Jha, S. N. & Lahiri, D. (2015). *J. Opt.* **44**, 182–194.
Ramanan, N., Lahiri, D., Garg, N., Bhattacharyya, D., Jha, S. N., Sahoo, N. K. & Sharma, S. M. (2012*b*). *J. Phys. Conf. Ser.* **377**, 012011.
Ruffoni, M. P. & Pettifer, R. F. (2006). *J. Synchrotron Rad.* **13**, 489–493.
Sahiner, M. A., Nabizadeh, A., Rivella, D., Cerqueira, L., Hachlica, J., Morea, R., Gonzalo, J. & Woicik, J. C. (2016). *J. Phys. Conf. Ser.* **712**, 012103.
Sanloup, C., Cochain, B., de Grouchy, C., Glazyrin, K., Konôpkova, Z., Liermann, H. P., Kantor, I., Torchio, R., Mathon, O. & Irifune, T. (2018). *J. Phys. Condens. Matter*, **30**, 084004.
Sharma, S. M. & Nandini Garg, N. (2017). *Materials Under Extreme Conditions – Recent Trends and Future Prospects*, ch. 1, pp. 1–47. Amsterdam: Elsevier.
Shen, G. & Mao, H. K. (2017). *Rep. Prog. Phys.* **80**, 016101.
Shimizu, Y., Tonooka, K., Yoshida, Y., Furuse, M. & Takashima, H. (2018). *Sci. Rep.* **8**, 15135.
Smith, J. S. & Desgreniers, S. (2009). *J. Synchrotron Rad.* **16**, 83–96.
Soignard, E., Benmore, C. J. & Yarger, J. L. (2010). *Rev. Sci. Instrum.* **81**, 035110.
Stoupin, S., Chung, E. H., Chattopadhyay, S., Segre, C. U. & Smotkin, E. S. (2006). *J. Phys. Chem. B*, **110**, 9932–9938.
Suzuki, Y., Kelly, S. D., Kemner, K. M. & Banfield, J. F. (2002). *Nature*, **419**, 134.
Tamura, S. (1972). *J. Mater. Sci.* **7**, 298–302.
Walsh, J. P. S. & Freedman, D. E. (2018). *Acc. Chem. Res.* **51**, 1315–1323.
Xu, J., Weng, X. J., Wang, X., Huang, J. Z., Zhang, C., Muhammad, H., Ma, X. & Liao, Q. D. (2013). *PLoS One*, **8**, e79289.
Zeng, Q., Ding, Y., Mao, W. L., Yang, W., Sinogeikin, S. V., Shu, J., Mao, H. & Jiang, J. Z. (2010). *Phys. Rev. Lett.* **104**, 105702.
Zibrov, I. P., Filonenko, V. P., Werner, P., Marinder, B. & Sundberg, M. (1998). *J. Solid State Chem.* **141**, 205–211.